LASER & PHOTONICS REVIEWS

www.lpr-journal.org

3D Engineering of Orbital Angular Momentum Beams via Liquid-Crystal Geometric Phase

Si-Jia Liu, Peng Chen, Shi-Jun Ge, Lin Zhu, Yi-Heng Zhang, and Yan-Qing Lu**

Orbital angular momentum (OAM) provides a novel degree of freedom for light, deeply inspiring versatile light-matter interactions and large-density multiplexing computing. Recently, multimode and multichannel control of OAM beams have aroused extensive curiosity, whereas their flexible engineering in 3D space still remains challenging. Here, a new type of liquid-crystal geometric phase optical elements is demonstrated to achieve on-demand 3D tailoring of OAM beams. Via integrating binary and continuous phase patterns into photo-aligned liquid crystals, customized 3D lattices of identical or propagation-variant OAM beams are generated in an electrically tunable broadband manner. By altering the incident spin, these volumetric OAM beams can be switched among different states on the higher-order Poincaré sphere. This work demonstrates a practical approach toward efficient OAM harnessing with large channel capacity and high spatial mode diversity, holding great potential for 3D optical manipulation, recording, and microscopy.

1. Introduction

Light proves to be an "all-rounder" on account of its abundant degrees of freedom (DOFs), such as amplitude, phase, wavelength, and polarization. In addition, the newly discovered orbital angular momentum (OAM) supplies an accessional DOF for light,[1–3] which has empowered numerous cutting-edge applications, including optical tweezers,[4] mode-division multiplexing classical and quantum computing,[5–7] and super-resolution microscopy.[8] Featured by a spiral phase front $e^{il\phi}$ and an OAM of $l\hbar$ per photon, the optical vortex is the most typical OAM-carrying beam, where l denotes the topological charge and ϕ is the azimuthal angle. Another category of OAM beams, the cylindrical vector beam,[9] stems from the superposition of optical vortices with opposite topological charges and orthogonal circular polarization. These different OAM beams can be mapped to respective points on the so-called "higher-order Poincaré (HOP) sphere."[10] Recently, multimode and multichannel tailoring of OAM beams have become two critical topics. The former desires higher mode complexity of each single OAM beam, such as vector vortex beams[11,12] and flower-shaped beams.[13,14] Meanwhile, the latter pursues arbitrary and parallel manipulation in higher spatial dimensions, creating diverse OAM beam arrays. So far, spatial light modulators,[15,16] metasurfaces,[17–21] and liquid crystals (LCs)[22,23] have been utilized to achieve multifarious OAM control. Among them, LC devices stand out as a promising candidate thanks to their high efficiency, stimuli responsiveness and cost-efficient mass production.

LCs refer to the intermediate matters between liquid and crystals. Owing to their intriguing electro-optical properties, LC devices have long been the dominator of the flat panel display market and have already become a rising star in the non-display field.[24,25] In particular, the LC-mediated geometric phase has drawn extensive attention in beam steering with regard to multiple DOFs.[26] The geometric phase, namely Pancharatnam–Berry (PB) phase, is correlated to photonic spin-orbit interaction and is usually proportional to the orientation angle of localized optical axes.[27] Common platforms for geometric phase modulation include LCs, metasurfaces,[19,20] and femtosecond laser written nanogratings.[28] Recently, such a spin-sensitive phase has been facilitating the innovation of LC planar elements, ranging from nematic-LC-based transmissive ones to chiral-LC-based reflective ones.[25,26] When it comes to the manipulation of OAM beams, several attempts have been made via LCs toward multimode and multichannel OAM harnessing.[29,30] However, those reported schemes are still restricted to low spatial dimensions and lacking in mode diversity, which significantly limits their potential in multiple optical tweezers,[31] 3D optical recording,[32] and parallel multiphoton microscopy.[33] Therefore, an LC element for 3D OAM beam engineering with improved capacity and flexibility is highly desired.

In this work, we propose and demonstrate a novel geometric phase optical element (GPOE) for 3D OAM beam engineering through photo-patterning LCs. Binary and continuous phase structures of a 2D Dammann grating (DG), a Dammann zone plate (DZP), a *q*-plate and an optional PB-lens are integrated by a noninterleaved design. Theoretically, Jones matrix calculation is exploited to analyze the functionality of the proposed LC GPOE. Experimentally, an OAM beam "cubic lattice" possessing

S.-J. Liu, P. Chen, S.-J. Ge, L. Zhu, Y.-H. Zhang, Y.-Q. Lu
National Laboratory of Solid State Microstructures
Key Laboratory of Intelligent Optical Sensing and Manipulation
College of Engineering and Applied Sciences
and Collaborative Innovation Center of Advanced Microstructures
Nanjing University
Nanjing 210093, P. R. China
E-mail: chenpeng@nju.edu.cn; yqlu@nju.edu.cn

The ORCID identification number(s) for the author(s) of this article can be found under https://doi.org/10.1002/lpor.202200118

DOI: 10.1002/lpor.202200118

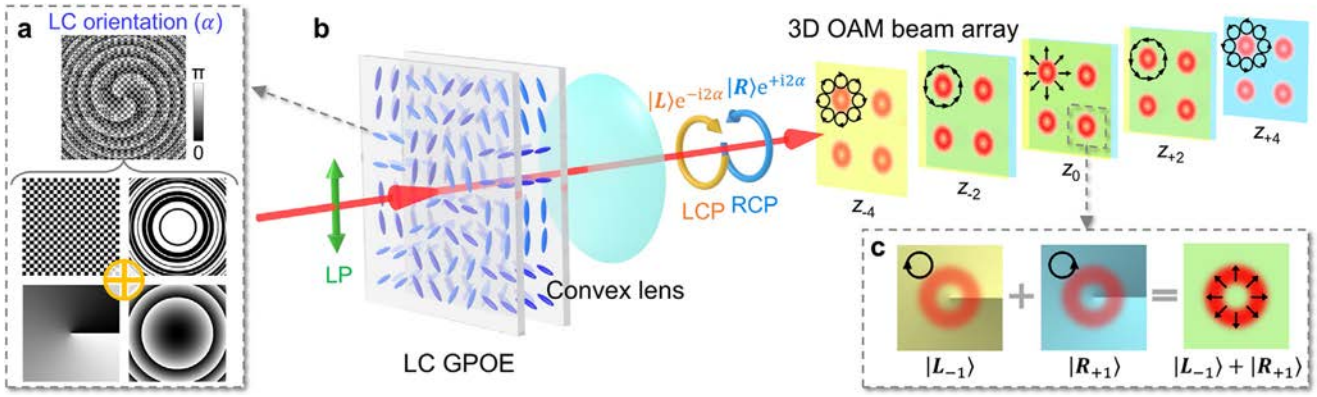

Figure 1. a) LC orientation distribution (α) of the proposed LC GPOE and its four components. The color varying from black to white corresponds to the LC orientation varying from 0 to π. b) Schematic generation of a space-variant 3D OAM beam array via the LC GPOE. Blue rods sandwiched by two glass substrates represent photo-patterned LC molecules. Colors of green, yellow, and blue represent linear polarization (LP), left circular polarization (LCP), and right circular polarization (RCP), respectively. Black arrows depict the localized polarization distributions. z_p refers to the distance between the p-th axial order and the convex lens. c) Illustration of the superposition of LCP and RCP optical vortices with $l = \pm 1$ into a radially polarized vector beam.

64 spin-sensitive channels is generated without imprinting the PB-lens. For the typical cases of circular and linear incident polarization, it can be switched between a 3D array of identical optical vortices and vector beams. Moreover, a 3D OAM beam array with modes varying across focal planes is created by rationally setting the focal length of the imprinted LC PB-lens. Optical vortices with opposite topological charges, radial and azimuthal vector beams are generated simultaneously in a spin-controllable and electrically-tunable broadband manner. Our proposed LC GPOEs exhibit high efficiency, good flexibility, and large channel capacity in OAM harnessing, and will open a promising avenue for soft matter photonics.

2. Design and Principle

Dammann encoding is a widely used technique for beam multiplying, enabling both transverse and axial beam arrays with an equal-energy distribution.[34,35] For example, by encoding a linear phase $2\pi x/\Lambda_x$ (Λ_x denoting the period) with the binary (0 or π) Dammann function ψ_M, a common DG with optimized phase transition points is formed, which can produce a $1 \times M$ array in the x-direction. When the quadratic phase of a Fresnel lens $\pi r^2/\lambda f$ ($r^2 = x^2 + y^2$, f denoting the focal length) is encoded with the same Dammann function, the so-called DZP is formed to generate M equal-energy focal points coaxially (see more details about Dammann encoding method in Note S1, Supporting Information).[36,37] Here, we imprint two binary and two continuous phase patterns of a 2D-DG, a DZP, a q-plate[38] and a PB-lens[39] into a single LC GPOE, as shown in **Figure 1**a. Its LC orientation distribution is expressed as

$$\begin{aligned}\alpha &= \alpha_{\mathrm{2D-DG}} + \alpha_{\mathrm{DZP}} + \alpha_{q-\mathrm{plate}} + \alpha_{\mathrm{PB-lens}} \\ &= \frac{1}{2}\left[\psi_M\left(\frac{2\pi x}{\Lambda_x}\right) + \psi_N\left(\frac{2\pi y}{\Lambda_y}\right)\right] \\ &\quad + \frac{1}{2}\psi_P\left(\frac{\pi r^2}{\lambda f}\right) + q\phi + \frac{\pi r^2}{2\lambda f_{\mathrm{PB}}} \end{aligned} \tag{1}$$

ψ_M, ψ_N, and ψ_P are the Dammann functions corresponding to M, N and P equal-energy orders. Λ_x, Λ_y, f and f_{PB} are the preset periods and focal lengths. q is the topological charge of the encoded q-plate, and the azimuthal angle $\phi = \arctan(y/x)$. The central region of this LC GPOE is vividly shown by the blue rods in Figure 1b.

The working principle of the proposed LC GPOE can be deduced by the Jones matrix calculation. Considering an arbitrarily polarized incident light, it can be described as the superposition of left and right circular polarization (LCP and RCP):

$$|\mathbf{u}_{\mathrm{in}}\rangle = \cos\left(\frac{\Theta}{2}\right)e^{-i\frac{\Phi}{2}}|\mathbf{L}\rangle + \sin\left(\frac{\Theta}{2}\right)e^{i\frac{\Phi}{2}}|\mathbf{R}\rangle \tag{2}$$

where (Θ, Φ) denotes the spherical coordinates of the common Poincaré sphere. $|\mathbf{L}\rangle = [1 \quad i]^{\mathrm{T}}/\sqrt{2}$ and $|\mathbf{R}\rangle = [1 \quad -i]^{\mathrm{T}}/\sqrt{2}$ represent LCP and RCP, respectively. After passing through the LC GPOE with a half-wave condition, the output light is expressed as

$$\begin{aligned}|\mathbf{u}_{\mathrm{out}}\rangle &= \mathbf{J}|\mathbf{u}_{\mathrm{in}}\rangle \\ &= \begin{bmatrix}\cos(2\alpha) & \sin(2\alpha) \\ \sin(2\alpha) & -\cos(2\alpha)\end{bmatrix}|\mathbf{u}_{\mathrm{in}}\rangle \\ &= \left[\cos\left(\frac{\Theta}{2}\right)e^{-i\frac{\Phi}{2}}|\mathbf{R}_{+2q}\rangle e^{i\frac{\pi r^2}{\lambda f_{\mathrm{PB}}}} + \sin\left(\frac{\Theta}{2}\right)e^{i\frac{\Phi}{2}}|\mathbf{L}_{-2q}\rangle e^{-i\frac{\pi r^2}{\lambda f_{\mathrm{PB}}}}\right] \\ &\quad \times \sum_{m=-\infty}^{+\infty}\sum_{n=-\infty}^{+\infty}\sum_{p=-\infty}^{+\infty} C_m C_n C_p e^{i\left(m\frac{2\pi x}{\Lambda_x} + n\frac{2\pi y}{\Lambda_y} + p\frac{\pi r^2}{\lambda f}\right)} \end{aligned} \tag{3}$$

$\mathbf{J}$ is the Jones matrix of the LC GPOE. $|\mathbf{R}_{+2q}\rangle = |\mathbf{R}\rangle e^{+i2q\phi}$ represents an RCP optical vortex with $l = +2q$, and $|\mathbf{L}_{-2q}\rangle = |\mathbf{L}\rangle e^{-i2q\phi}$ represents an LCP optical vortex with $l = -2q$. C_m, C_n, and C_p are the optimized complex coefficients of the (m-th, n-th) transverse order and the p-th axial order. Equation (3) indicates the high flexibility for 3D OAM beam tailoring (see more detailed derivation in Note S2, Supporting Information). With the aid of a convex

lens, both real and virtual focal planes (corresponding to negative and positive p values) of the output light can be extracted near the lens focus. For the extreme case of $f_{PB} \to \infty$, i.e., without imprinting the PB-lens, the output turns out to be a spin-dependent $M\times N\times P$ OAM beam lattice with identical OAM modes. 3D optical vortex arrays of $|\mathbf{R}_{+2q}\rangle$ and $|\mathbf{L}_{-2q}\rangle$ can be generated at the same location for $|\mathbf{u}_{in}\rangle = |\mathbf{L}\rangle$ and $|\mathbf{u}_{in}\rangle = |\mathbf{R}\rangle$, respectively. While for linear polarization (LP), cylindrical vector beams will appear due to the superposition of $|\mathbf{R}_{+2q}\rangle$ and $|\mathbf{L}_{-2q}\rangle$ at each diffraction order.

When f_{PB} takes finite values, the LCP and RCP components of the incident light acquire opposite additional phase of $\pm\pi r^2/\lambda f_{PB}$, thus evolving into two axially-shifted $M \times N \times P$ optical vortex arrays. Notably, in some special cases, these two axially shifted arrays overlap again in certain orders and will result in a propagation-variant OAM beam array. For example, when $f_{PB} = f$, the output follows the expression:

$$|\mathbf{u}_{out}\rangle = \sum_{p=-\infty}^{+\infty} \left[\cos\left(\frac{\Theta}{2}\right) e^{-i\frac{\Phi}{2}} C_{p-1} |\mathbf{R}_{+2q}\rangle + \sin\left(\frac{\Theta}{2}\right) e^{i\frac{\Phi}{2}} C_{p+1} |\mathbf{L}_{-2q}\rangle \right] e^{ip\frac{\pi r^2}{\lambda f}} \times \sum_{m=-\infty}^{+\infty} \sum_{n=-\infty}^{+\infty} C_m C_n e^{i\left(m\frac{2\pi x}{\Lambda_x} + n\frac{2\pi y}{\Lambda_y}\right)} \quad (4)$$

In this case, 3D arrays of $|\mathbf{R}_{+2q}\rangle$ and $|\mathbf{L}_{-2q}\rangle$ are oppositely shifted by exactly one axial order, with C_{p-1} and C_{p+1} becoming their coefficients at z_p (the p-th axial order). For LP incident light, as illustrated in Figure 1b, the overlapped diffraction orders construct cylindrical vector beams, while the non-overlapped ones remain optical vortices, thereby forming an $M\times N\times(P+1)$ space-variant OAM beam lattice. Figure 1c depicts the construction of a radially polarized beam by overlapping LCP and RCP optical vortices with $l = \pm 1$. Through designing the phase difference between C_{p-1} and C_{p+1}, which contributes to the relative phase between $|\mathbf{R}_{+2q}\rangle$ and $|\mathbf{L}_{-2q}\rangle$ at z_p, vector beams with various polarization distributions[10] can be obtained in different focal planes.

3. Results and Discussion

Figure 2a exhibits the orientation distribution of an LC GPOE (5.3 mm × 5.3 mm) without encoding a PB-lens, which integrates a 2D-DG ($\Lambda_x = \Lambda_y = 540$ μm, $M = N = 4$), a DZP ($f = 225$ cm for $\lambda = 632.8$ nm, $P = 4$), and a q-plate ($q = 0.5$). In experiments, the in-plane variant LC orientation was realized via dynamic photopatterning technology.[40] Two indium-tin-oxide glass substrates spin-coated with the photo-alignment agent SD1[41] were glued together with a cell gap of 8 μm. Then, the cell was exposed to polarized UV light by a multistep partly overlapping method, after which nematic LC E7 was filled in to achieve the designed LC GPOE. Under crossed polarizers, the micrograph of the central region of the fabricated GPOE is shown in Figure 2b. The spiral structure provided by the imprinted q-plate contributes to the azimuthally varying brightness, while the binary structures of the 2D-DG and DZP result in square and circular disclination lines, respectively. Figure 2c illustrates the optical setup to generate and analyze the spin-dependent 3D OAM beam array. L_1 ($f_1 = 5$ cm) and L_2 ($f_2 = 25$ cm) constitute a beam expander to get a beam diameter of 5 mm. P_1 together with the wave plate is utilized to control the incident polarization. Convex lens L_3 ($f_3 = 10$ cm) is adopted to extract the generated virtual focal planes to real regions. A CCD is mounted on a linear translation stage to capture the diffraction patterns in different focal planes.

To keep the half-wave condition for the incident wavelength (632.8 nm), a 1 kHz square-wave signal with a voltage of 2.9 V is applied to the LC GPOE. When $|\mathbf{u}_{in}\rangle = |\mathbf{L}\rangle$ as shown in Figure 2d (see magnified images in Figure S1a, Supporting Information), a 4 × 4 × 4 optical vortex lattice of $|\mathbf{R}_{+1}\rangle$ is efficiently generated, with donut-like intensity profiles located at the periodic lattice nodes in different focal planes ($z_{-3} = 8.8$ cm, $z_{-1} = 9.6$ cm, $z_{+1} = 10.5$ cm, and $z_{+3} = 11.5$ cm). By interfering with a plane wave at z_{+1}, the 4 × 4 optical vortices with identical $l = +1$ are well verified according to the number and direction of the fork-shaped fringes (Figure 2f) (see interferometric results in each focal plane in Figure S1b, Supporting Information). As for horizontal LP incident light ($|\mathbf{u}_{in}\rangle = (|\mathbf{L}\rangle + |\mathbf{R}\rangle)/\sqrt{2}$), a 4 × 4 × 4 array of radially polarized beams ($(|\mathbf{R}_{+1}\rangle + |\mathbf{L}_{-1}\rangle)/\sqrt{2}$) is obtained at the same location (Figure 2e; see magnified images in Figure S1c, Supporting Information). The polarization distribution of this 64-channel 3D vector beam array is detected by inserting an analyzer P_2. Take $z = z_{-3}$ for example, lobed structures consistently parallel to the transmission axis of P_2 are observed in Figure 2g, indicating the identical radial polarization. Additionally, large-capacity 3D arrays of identical LCP optical vortices or other vector beams can also be created by altering the incident polarization.

Through further imprinting a PB-lens with $f_{PB} = f$, a space-variant 3D OAM beam array can be expected according to Equation (4). Here, another LC GPOE is designed by incorporating a 2D-DG ($\Lambda_x = \Lambda_y = 196$ μm, $M = N = 2$), a DZP ($f = 150$ cm for $\lambda = 632.8$ nm, $P = 4$), a q-plate ($q = 0.5$) and a PB-lens ($f_{PB} = 150$ cm for $\lambda = 632.8$ nm), whose LC orientation distribution is shown in the middle of **Figure 3**a. Notably, for the imprinted DZP, the involved Dammann function ψ_4 is optimized with both reflection and translation symmetry,[42] leading to four equal-energy axial orders (C_{-3}, C_{-1}, C_{+1}, and C_{+3}) with the respective phase of either $-\pi/2$ or $\pi/2$ (Figure 3b). Localized micrographs of this LC GPOE are exhibited in Figure 3a. Continuously variant brightness and regular disclination lines are also observed, but the fan-shaped pattern in Figure 2b changes into an "S"-shaped pattern due to the additionally imprinted PB-lens. In optical characterization, for $|\mathbf{u}_{in}\rangle = |\mathbf{L}\rangle$, an axially shifted 2 × 2 × 4 optical vortex array of $|\mathbf{R}_{+1}\rangle$ is generated at $z_{-2} = 8.8$ cm, $z_0 = 10.0$ cm, $z_{+2} = 11.5$ cm, and $z_{+4} = 13.3$ cm (Figure 3d; see magnified images in Figure S2a, Supporting Information), which is well confirmed by interferometric measurements (Figure S2b, Supporting Information). Its theoretical intensity spectrum of $|C_{p-1}|^2$ and phase spectrum of $\arg(C_{p-1})$ at different z_p are calculated in Figure 3c, showing a one-order shift compared to that in Figure 3b. While for $|\mathbf{u}_{in}\rangle = |\mathbf{R}\rangle$, a 2 × 2 × 4 optical vortex array of $|\mathbf{L}_{-1}\rangle$ is observed at $z_{-4} = 7.8$ cm, z_{-2}, z_0, and z_{+2} (Figure 3f; see magnified images and interferometric measurements in Figure S2c,d, Supporting Information), with an oppositely shifted spectrum of $|C_{p+1}|^2$ and $\arg(C_{p+1})$ (Figure 3e).

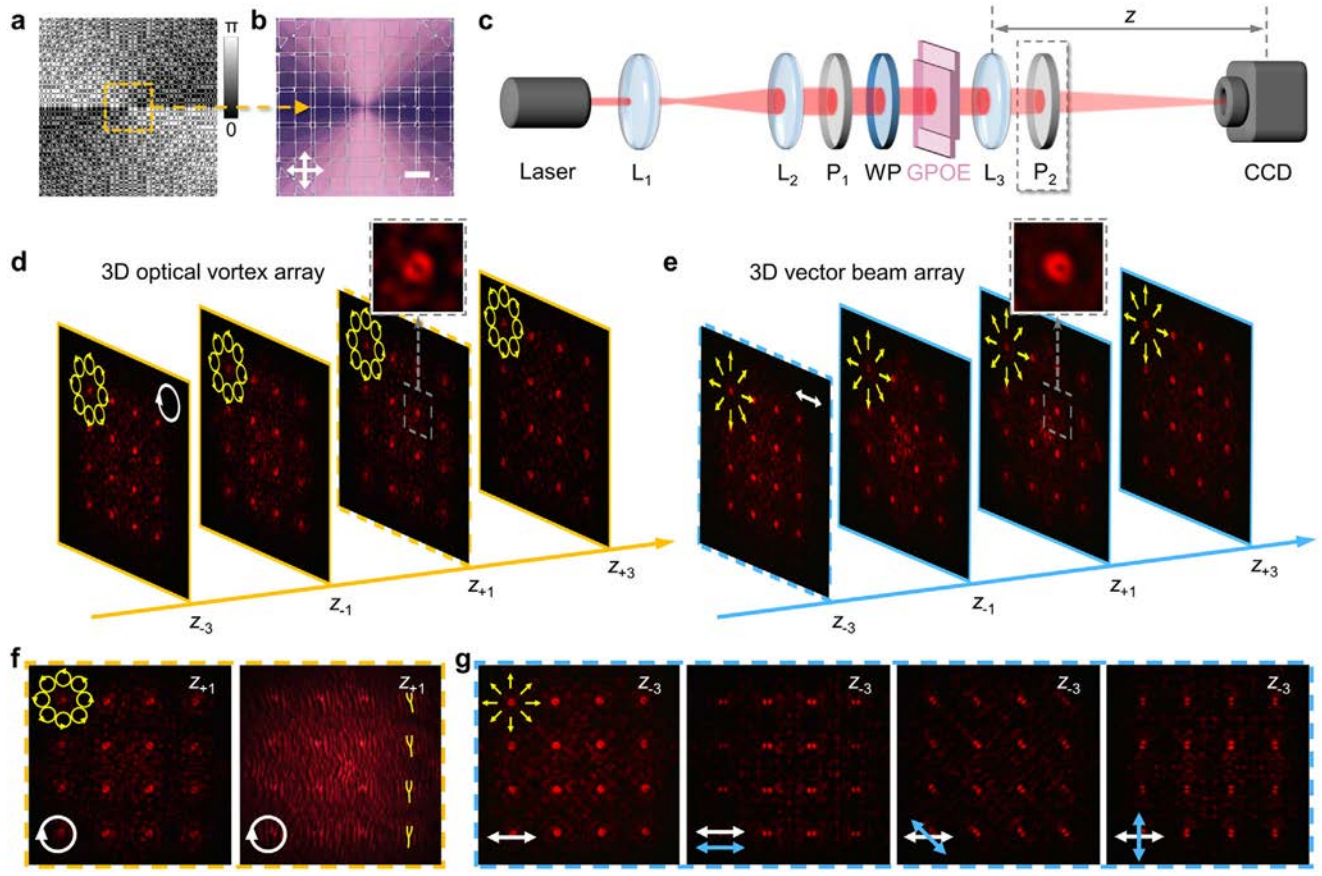

Figure 2. a) Designed orientation distribution of the LC GPOE without imprinting a PB-lens. b) Micrograph of the central region of (a) under a polarized optical microscope. Crossed white arrows represent the orthogonal polarizer and analyzer. The scale bar is 200 μm. c) Optical setup to generate and analyze the 3D OAM beam array. L_1 and L_2, lenses for beam expanding; P_1 and P_2, polarizer and analyzer; WP, half-wave plate or quarter-wave plate; L_3, convex lens for extracting virtual focal planes; CCD, charge-coupled device. z refers to the distance between CCD and L_3. Diffraction patterns in desired focal planes of d) a 4 × 4 × 4 optical vortex array and e) a 4 × 4 × 4 vector beam array generated by LCP and horizontal LP incident light, respectively. Insets are enlarged patterns of the selected diffraction order. White and yellow arrows represent the incident and output polarization distributions. f) Diffraction pattern and corresponding interferometric result captured at z_{+1} of (d). The fork-shaped fringes after interference with a plane wave are marked by yellow lines. g) Diffraction pattern and polarization detection results captured at z_{-3} of (e), with blue arrows labeling the different transmission directions of P_2.

Particularly, for LP incident light, the diffraction patterns can be viewed as the superposition of Figure 3d,f. Take vertical LP ($|\mathbf{u}_{in}\rangle = \mathrm{i}(-|\mathbf{L}\rangle + |\mathbf{R}\rangle)/\sqrt{2}$) for example, Figure 3h shows the generated 2 × 2 × 5 space-variant OAM beam array (see magnified images in Figure S3a, Supporting Information). According to Equation (4), the corresponding OAM mode at z_p is given by $\mathrm{i}(-C_{p-1}|\mathbf{R}_{+1}\rangle + C_{p+1}|\mathbf{L}_{-1}\rangle)/\sqrt{2}$. At z_{-4} and z_{+4}, 2×2 optical vortex arrays of $|\mathbf{L}_{-1}\rangle$ and $|\mathbf{R}_{+1}\rangle$ are preserved, respectively, which can be mapped to the south and north pole of the HOP sphere in Figure 3g. While at z_{-2}, z_0, and z_{+2}, $|\mathbf{R}_{+1}\rangle$ and $|\mathbf{L}_{-1}\rangle$ totally coincide and construct cylindrical vector beams, whose localized polarization distributions are determined by the relative phase between $|\mathbf{R}_{+1}\rangle$ and $|\mathbf{L}_{-1}\rangle$. Considering the complex spectrum of C_{p-1} and C_{p+1} (Figure 3c,e), the relative phase at z_{-2} and z_{+2} is calculated to be π, resulting in azimuthally polarized vector beams, while the relative phase of 0 at z_0 gives rise to the radial polarization. These two orthogonal OAM modes can be mapped to the equator of the HOP sphere (Figure 3g). In total, four typical HOP sphere states are created simultaneously in a propagation-variant way. Figure 3i presents the detection results in different focal planes. Interferometric measurement is also adopted to detect the l of optical vortices, and $l = -1$ at z_{-4} and $l = +1$ at z_{+4} are identified, respectively. P_2 is inserted to analyze the polarization distributions of the generated vector beams. Lobed structures at z_{-2} and z_{+2} keep perpendicular to the transmission direction of P_2, verifying the azimuthal polarization. Meanwhile, lobes at z_0 are parallel to the direction of P_2, indicating the radial polarization. Actually, this spin-controllable LC GPOE can achieve any state on the HOP sphere, holding great potential for 3D OAM tailoring.

The inherent achromaticity of the geometric phase and the electro-optical tunability of LC materials promise the adaptable working wavelength for the proposed GPOEs. Accordingly, the sample in Figure 3a is further investigated at 532 nm via adjusting the half-wave voltage to 3.3 V. For horizontal LP incident light, **Figure 4**a presents the generated high-quality 2 × 2 × 5 space-variant OAM beam array, whose focal planes move to z_{-4} = 8.1 cm, z_{-2} = 9.0 cm, z_0 = 10.0 cm, z_{+2} = 11.2 cm, and

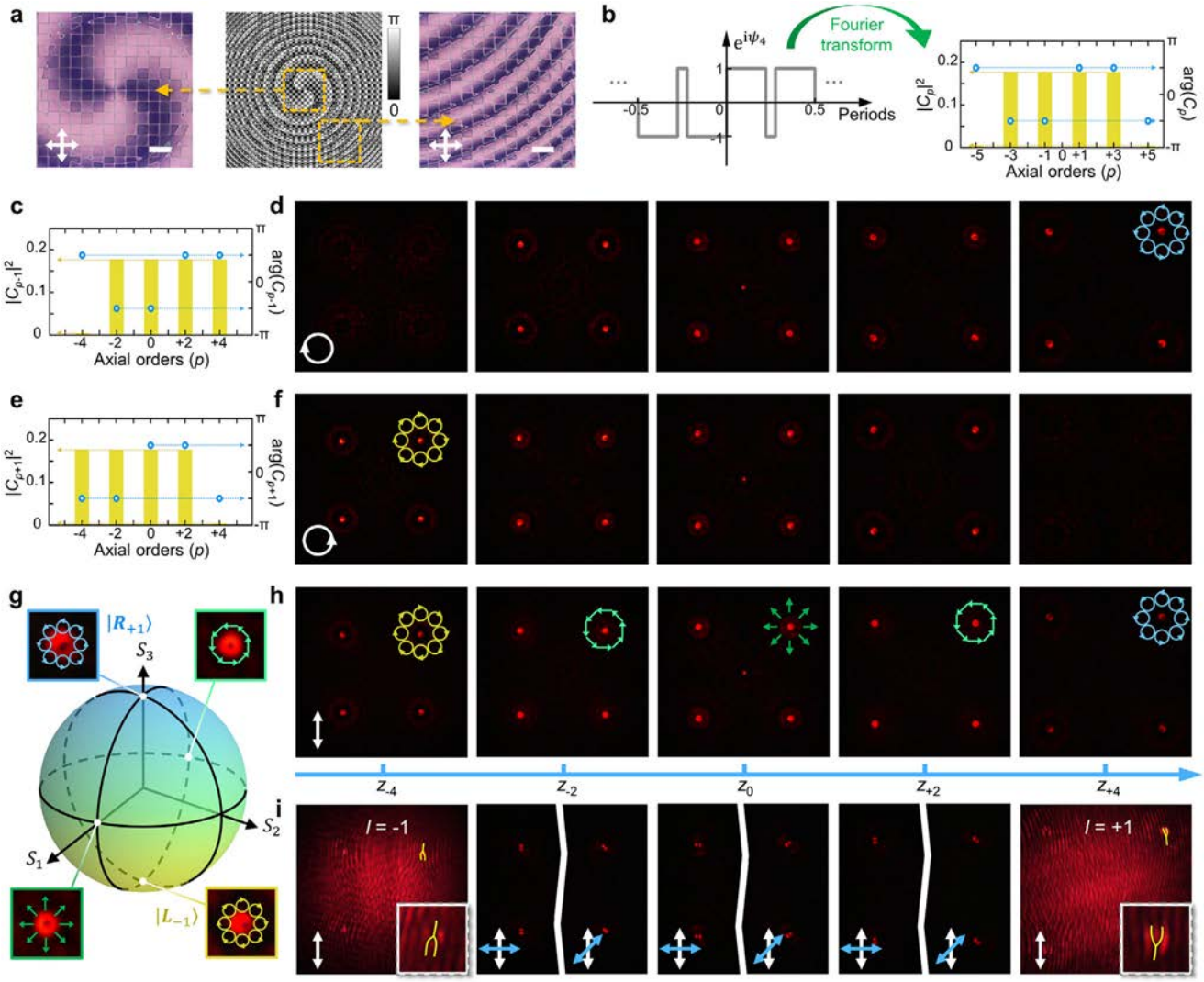

Figure 3. a) Designed orientation distribution and localized micrographs of the PB-lens-imprinted LC GPOE. All scale bars are 200 μm. b) Optimized Dammann function corresponding to four equal-energy orders and its Fourier spectrum. Normalized phase transition points are selected as 0, 0.2228, 0.2772, 0.5, 0.7228, and 0.7772. Yellow bars depict the normalized intensity spectrum, while blue circles depict the phase spectrum. Diffraction patterns of d) RCP and f) LCP 2 × 2× 4 optical vortex arrays, with axially shifted intensity and phase spectrum shown in c) and e). White and colored arrows represent incident and output polarization distributions, respectively. h) 2 × 2 × 5 space-variant OAM beam array generated by vertical LP incident light, whose OAM modes correspond to four different points on g) a HOP sphere. Insets are enlarged patterns of different OAM beams from different focal planes in (h). i) Detection results of (h) with interferometry or an analyzer labeled by blue arrows. Yellow lines mark the fork-shaped fringes after interference with a plane wave at z_{-4} and z_{+4}.

z_{+4} = 12.7 cm (see magnified images in Figure S3b, Supporting Information). This array is also composed of LCP and RCP optical vortices, and azimuthally and radially polarized beams, but the latter two vector beams exchange their locations compared with Figure 3h due to the orthogonal incident LP. The anticipated polarization distributions are confirmed by the polarization detection results at z_{-2}, z_0, and z_{+2} (Figure 4b). Moreover, the relative intensity distribution of the generated 3D OAM beam array is measured. As shown in Figure 4c, good uniformity is observed in each focal plane and the intensity at z_{-4} and z_{+4} is about half of that at z_{-2}, z_0, and z_{+2}, matching well with the theoretical analysis. Some scattered light and imperfections of the diffraction can be attributed to the influence of those unfocused orders and fabrication deviations from the ideal structure, decreasing the overall efficiency. This issue can be well improved by employing the photo-patterning system with much higher resolution and further optimizing the structure design.

4. Conclusion

In summary, flexible OAM beam tailoring in 3D space has been realized via the LC-mediated geometric phase. Through integrating several customized phase structures, spin-controllable 3D OAM beam arrays with identical or space-variant OAM modes are generated with high quality and large capacity. A shift-and-overlap method is proposed to improve the mode diversity of 3D

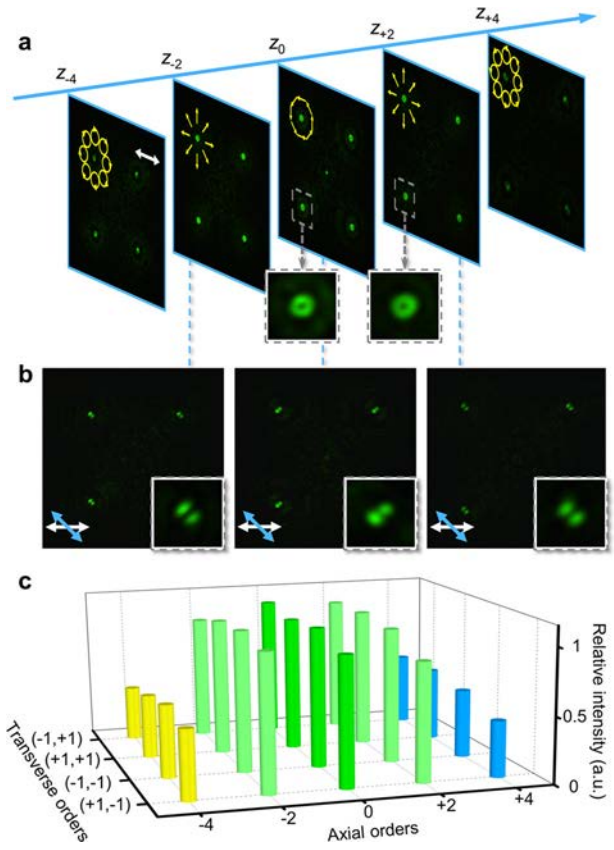

Figure 4. a) $2 \times 2 \times 5$ space-variant OAM beam array at 532 nm. b) Polarization detection results of (a) at z_{-2}, z_0 and z_{+2}. Blue arrows indicate the transmission direction of the analyzer. Insets are enlarged lobed intensity profiles in corresponding focal planes. c) Relative intensity distribution of the diffraction orders in (a).

OAM beam lattices, and four typical HOP sphere states are produced simultaneously as an example. Actually, this method can be extended to arbitrary directions, such as transverse and radial ones, which may enlighten more delicate designs. Besides, the interleaving scheme[43,44] and the idea of spatial harmonic beating[45] can also be introduced to achieve 3D control of OAM beams. Compared with other material systems, our proposed LC GPOEs are distinguished by cost-efficient fabrication, electrical tunability, and dynamic switchability. This work provides a versatile platform for multifunctional OAM harnessing via preprogrammed LCs, facilitating 3D operation in optical manipulation, recording and microscopy.

Supporting Information

Supporting Information is available from the Wiley Online Library or from the author.

Acknowledgements

This work was supported by the National Key R&D Program of China (No. 2021YFA1202000), the National Natural Science Foundation of China (NSFC) (Nos. 12004175, 62175101, and 62105143), the Natural Science Foundation of Jiangsu Province (Nos. BK20212004, BK20200311 and BK20210179), the Fundamental Research Funds for the Central Universities (No. 021314380185), and the Innovation and Entrepreneurship Program of Jiangsu Province. [Correction added on 15 June 2022, after initial publication: In Equations 2, 3, and 4, various Greek symbols were incorrect in the pdf and have now been corrected.]

Conflict of Interest

The authors declare no conflict of interest.

Data Availability Statement

The data that support the findings of this study are available from the corresponding author upon reasonable request.

Keywords

geometric phases, liquid crystals, orbital angular momentum beams, three-dimensional arrays

Received: March 11, 2022
Published online: May 9, 2022

[1] L. Allen, M. W. Beijersbergen, R. J. C. Spreeuw, J. P. Woerdman, *Phys. Rev. A* **1992**, *45*, 8185.
[2] Y. J. Shen, X. J. Wang, Z. W. Xie, C. J. Min, X. Fu, Q. Liu, M. L. Gong, X. C. Yuan, *Light: Sci. Appl.* **2019**, *8*, 90.
[3] J. Chen, C. H. Wan, Q. W. Zhan, *Adv. Photonics* **2021**, *3*, 064001.
[4] D. L. Gao, W. Q. Ding, M. Nieto-Vesperinas, X. M. Ding, M. Rahman, T. H. Zhang, C. Lim, C. W. Qiu, *Light: Sci. Appl.* **2017**, *6*, 17039.
[5] A. E. Willner, H. Huang, Y. Yan, Y. Ren, N. Ahmed, G. Xie, C. Bao, L. Li, Y. Cao, Z. Zhao, J. Wang, M. P. J. Lavery, M. Tur, S. Ramachandran, A. F. Molisch, N. Ashrafi, S. Ashrafi, *Adv. Opt. Photonics* **2015**, *7*, 66.
[6] M. Erhard, R. Fickler, M. Krenn, A. Zeilinger, *Light: Sci. Appl.* **2018**, *7*, 17146.
[7] X. Y. Fang, H. R. Ren, K. Y. Li, H. T. Luan, Y. L. Hua, Q. M. Zhang, X. Chen, M. Gu, *Adv. Opt. Photonics* **2021**, *13*, 772.
[8] G. Vicidomini, P. Bianchini, A. Diaspro, *Nat. Methods* **2018**, *15*, 173.
[9] Q. W. Zhan, *Adv. Opt. Photonics* **2009**, *1*, 1.
[10] G. Milione, H. I. Sztul, D. A. Nolan, R. R. Alfano, *Phys. Rev. Lett.* **2011**, *107*, 053601.
[11] Z. X. Liu, Y. Y. Liu, Y. G. Ke, Y. C. Liu, W. X. Shu, H. L. Luo, S. C. Wen, *Photonics Res* **2017**, *5*, 15.
[12] Y. J. Bao, J. C. Ni, C. W. Qiu, *Adv. Mater.* **2020**, *32*, 1905659.
[13] T. H. Lu, T. D. Huang, J. G. Wang, L. W. Wang, R. R. Alfano, *Sci. Rep.* **2016**, *6*, 39657.
[14] H. H. Fan, H. Zhang, C. Y. Cai, M. M. Tang, H. H. Li, J. Tang, X. Z. Li, *Ann. Phys.* **2021**, *533*, 2000575.
[15] C. Rosales-Guzmán, N. Bhebhe, A. Forbes, *Opt. Express* **2017**, *25*, 25697.
[16] S. Y. Fu, T. L. Wang, Z. Y. Zhang, Y. W. Zhai, C. Q. Gao, *Appl. Phys. Lett.* **2017**, *110*, 191102.
[17] A. Arbabi, Y. Horie, M. Bagheri, A. Faraon, *Nat. Nanotechnol.* **2015**, *10*, 937.
[18] L. L. Huang, X. Song, B. Reineke, T. Y. Li, X. W. Li, J. Liu, S. Zhang, Y. T. Wang, T. Zentgraf, *ACS Photonics* **2017**, *4*, 338.
[19] F. Y. Yue, D. D. Wen, C. M. Zhang, B. D. Gerardot, W. Wang, S. Zhang, X. Z. Chen, *Adv. Mater.* **2017**, *29*, 1603838.

[20] E. L. Wang, L. N. Shi, J. B. Niu, Y. L. Hua, H. L. Li, X. L. Zhu, C. Q. Xie, T. C. Ye, *Adv. Opt. Mater.* **2019**, *7*, 1801415.
[21] Z. H. Jiang, L. Kang, T. W. Yue, H. X. Xu, Y. J. Yang, Z. W. Jin, C. Y. Yu, W. Hong, D. H. Werner, C. W. Qiu, *Adv. Mater.* **2020**, *32*, 1903983.
[22] P. Chen, S. J. Ge, W. Duan, B. Y. Wei, G. X. Cui, W. Hu, Y. Q. Lu, *ACS Photonics* **2017**, *4*, 1333.
[23] C. T. Xu, P. Chen, Y. H. Zhang, X. Y. Fan, Y. Q. Lu, W. Hu, *Appl. Phys. Lett.* **2021**, *118*, 151102.
[24] J. H. Xiong, S.-T. Wu, *eLight* **2021**, *1*, 3.
[25] N. V. Tabiryan, D. E. Roberts, Z. Liao, J. Y. Hwang, M. Moran, O. Ouskova, A. Pshenichnyi, J. Sigley, A. Tabirian, R. Vergara, L. D. Sio, B. R. Kimball, D. M. Steeves, J. Slagle, M. E. McConney, T. J. Bunning, *Adv. Opt. Mater.* **2021**, *9*, 2001692.
[26] P. Chen, B. Y. Wei, W. Hu, Y. Q. Lu, *Adv. Mater.* **2020**, *32*, 1903665.
[27] E. Cohen, H. Larocque, F. Bouchard, F. Nejadsattari, Y. Gefen, E. Karimi, *Nat. Rev. Phys.* **2019**, *1*, 437.
[28] R. Drevinskas, P. G. Kazansky, *APL Photonics* **2017**, *2*, 066104.
[29] P. Chen, S. J. Ge, L. L. Ma, W. Hu, V. Chigrinov, Y. Q. Lu, *Phys. Rev. Appl.* **2016**, *5*, 044009.
[30] Y. H. Zhang, P. Chen, S. J. Ge, T. Wei, J. Tang, W. Hu, Y. Q. Lu, *Appl. Phys. Lett.* **2020**, *117*, 081101.
[31] N. Bhebhe, P. A. C. Williams, C. Rosales-Guzman, V. Rodriguez-Fajardo, A. Forbes, *Sci. Rep.* **2018**, *8*, 17387.
[32] X. P. Li, Y. Y. Cao, N. Tian, L. Fu, M. Gu, *Optica* **2015**, *2*, 567.
[33] M. Gu, H. Lin, X. P. Li, *Opt. Lett.* **2013**, *38*, 3627.
[34] H. Dammann, E. Klotz, *Opt. Acta* **1977**, *24*, 505.
[35] I. Moreno, J. A. Davis, D. M. Cottrell, N. Zhang, X. C. Yuan, *Opt. Lett.* **2010**, *35*, 1536.
[36] J. J. Yu, C. H. Zhou, W. Jia, W. G. Cao, S. Q. Wang, J. Y. Ma, H. C. Cao, *Appl. Opt.* **2012**, *51*, 1619.
[37] J. J. Yu, C. H. Zhou, W. Jia, A. D. Hu, W. G. Cao, J. Wu, S. Q. Wang, *Appl. Opt.* **2012**, *51*, 2485.
[38] L. Marrucci, C. Manzo, D. Paparo, *Phys. Rev. Lett.* **2006**, *96*, 163905.
[39] C. P. Jisha, S. Nolte, A. Alberucci, *Laser Photonics Rev.* **2021**, *15*, 2100003.
[40] P. Chen, L. L. Ma, W. Duan, J. Chen, S. J. Ge, Z. H. Zhu, M. J. Tang, R. Xu, W. Gao, T. Li, W. Hu, Y. Q. Lu, *Adv. Mater.* **2018**, *30*, 1705865.
[41] H. Akiyama, T. Kawara, H. Takada, H. Takatsu, V. Chigrinov, E. Prudnikova, V. Kozenkov, H. Kwok, *Liq. Cryst.* **2002**, *29*, 1321.
[42] R. L. Morrison, *J. Opt. Soc. Am. A* **1992**, *9*, 464.
[43] D. M. Lin, A. L. Holsteen, E. Maguid, G. Wetzstein, P. G. Kik, E. Hasman, M. L. Brongersma, *Nano Lett.* **2016**, *16*, 7671.
[44] D. M. Lin, A. L. Holsteen, E. Maguid, P. Y. Fan, P. G. Kik, E. Hasman, M. L. Brongersma, *Opt. Express* **2018**, *26*, 24835.
[45] A. H. Dorrah, N. A. Rubin, A. Zaidi, M. Tamagnone, F. Capasso, *Nat. Photonics* **2021**, *15*, 287.